Hotspot-mediated non-dissipative and ultrafast plasmon passage

Eva-Maria Roller[1][†], Lucas V. Besteiro[2][†], Claudia Pupp[1], Larousse Khosravi Khorashad[2], Alexander O. Govorov[2]* and Tim Liedl[1]*

Plasmonic nanoparticles hold great promise as photon handling elements and as channels for coherent transfer of energy and information in future all-optical computing devices[1–5]. Coherent energy oscillations between two spatially separated plasmonic entities via a virtual middle state exemplify electron-based population transfer, but their realization requires precise nanoscale positioning of heterogeneous particles[6–10]. Here, we show the assembly and optical analysis of a triple-particle system consisting of two gold nanoparticles with an inter-spaced silver island. We observe strong plasmonic coupling between the spatially separated gold particles, mediated by the connecting silver particle, with almost no dissipation of energy. As the excitation energy of the silver island exceeds that of the gold particles, only quasi-occupation of the silver transfer channel is possible. We describe this effect both with exact classical electrodynamic modelling and qualitative quantum-mechanical calculations. We identify the formation of strong hotspots between all particles as the main mechanism for the lossless coupling and thus coherent ultrafast energy transfer between the remote partners. Our findings could prove useful for quantum gate operations, as well as for classical charge and information transfer processes.

Low-dissipative transfer of excitations over short and long distances is at the heart of information science as well as energy harvesting. Energy transfer processes, for example, play a key role in highly efficient dipolar interactions in the light harvesting complexes of chloroplasts, and low-loss exciton transport is sought after in solar cell development. Both Förster-resonance energy transfer (FRET) in biomolecular systems and diffusion of excitons in solar cells are incoherent processes, and therefore often dissipative. Also information inside computer chips is, as of today, processed and transferred incoherently. On the other hand, coherence is a crucial feature in interferometry, and indispensable in future quantum computation.

With the goal to achieve fast and coherent transfer between nanoscale components, a variety of quantum approaches has emerged. Generally, quantum-mechanical tunnelling is fast enough to avoid inelastic scattering during the passage, which makes it a low-loss process that is widely used in modern electronic technology. In particular, chains of potential wells were proposed for tunnelling by adiabatic passage (CTAP)[1,2] and optical stimulated Raman adiabatic passage (STIRAP) has been realized by transferring spin populations of two long-living quantum states via an optical third state[11,12].

Another approach for transport of information at the nanoscale is the use of plasmonic components[13]. Plasmons are coherent, but they are usually dissipative and have only short lifetimes. Both disadvantages are the result of the high scattering probability of electrons in metals, which hampers the use of plasmonic waveguides for transfer applications. Inspired by efforts to exploit quantum-mechanical mechanisms we now propose a particle trimer system where plasmons are coherently transferred over extended distances. The system consists of two identical but spatially separated nanoparticles of one type and a third intermediate nanoparticle of a different type, the latter exhibiting also a different energetic level. The plasmons are transferred between the identical nanoparticles via the third nanoparticle, even with the two identical particles being too far away from each other to couple directly.

The experimental realization of such a plasmon-based transfer system requires full control over spatial organization of heterogeneous nanoparticles. DNA-based self-assembly offers the possibility to fabricate nanoscale objects that can accommodate inorganic particles at extremely well defined positions with high yields[6–9,14–17]. Previous assemblies with DNA-based templates consist of arrays[8], chain-like[18,19], helical[9], or ring shaped[20] arrangements of metal nanoparticles, as well as chains of dyes[21] and quantum dots[22,23]. Owing to the possibility of functionalizing particle species with orthogonal DNA sequences—that is, sequences that do not interfere with each other—heterogeneous particle architectures have been realized, including dimers and trimers[23,24], lattices[8], core-satellites[15,25] and rings[20]. Lithographical attempts to build plasmonic devices from heterogeneous metals consist of bimetallic nanodot arrays[26] and nanoantenna dimers of gold and silver disks[27]. However, top-down approaches suffer from limited spatial control on the scale below tens of nanometres, and generally result in less homogeneous crystalline structures made of sputtered or epitaxially deposited materials. Colloidal nanoparticles, in contrast, exhibit high crystalline quality and sharp size distributions.

To overcome the limitations of top-down lithography, we here use a DNA origami structure to spatially arrange gold and silver nanoparticles (AuNPs and AgNPs) in heterotrimers with nanometre precision and high assembly yields[28–30]. Our DNA origami template consists of a cylindrical 14-helix bundle (for design details and assembling procedures, see Methods and Supplementary Fig. 1), which offers lengthwise three equally spaced sequence-specific attachment sites for DNA-functionalized nanoparticles. AuNPs functionalized with a DNA sequence complementary to the outer sites and one AgNP functionalized with a sequence complementary to the middle site were hybridized to each origami template (Fig. 1a). The resulting heterogeneous nanoparticle trimer displays a designed interparticle gap of 40 nm between the two outer AuNPs, with the AgNP accommodated in between. After assembly, we confirmed
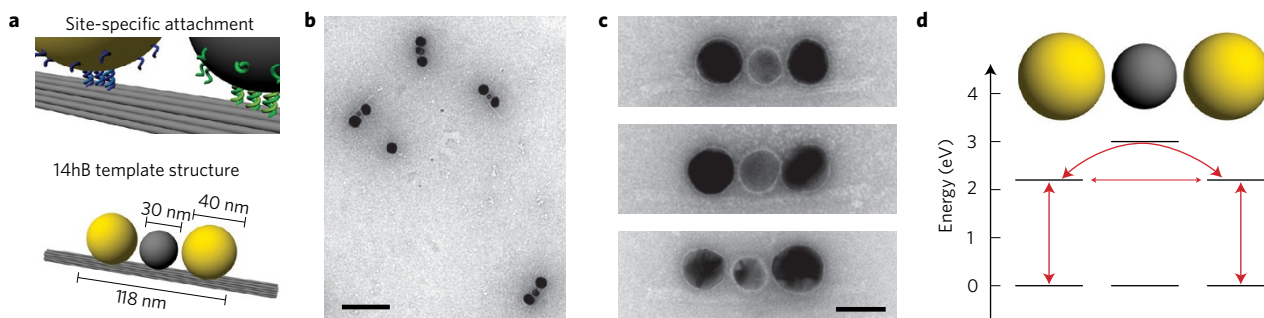
761

Figure 1 | Plasmonic transfer system. a, Design scheme of the DNA origami-templated heterogeneous trimer structure. AuNPs and AgNPs bind via specific DNA sequences (shown in blue and green) to designated sites on the DNA origami structure. **b**, Wide-field TEM image of the assembled heterotrimers. Scale bar, 200 nm. **c**, High-magnification TEM images reveal the two outer AuNPs, the middle AgNP and the DNA origami scaffold. Scale bar, 40 nm. **d**, Energy scheme and concept of the plasmonic transfer system. The middle Ag particle serves as a virtual transmitter connecting the two separated Au particles.

this configuration by transmission electron microscopy (TEM) (Fig. 1b,c, Methods and Supplementary Fig. 2). Note that the AgNPs in our experiments are slightly smaller than the AuNPs and exhibit less contrast.

Conceptually, the distance between the AuNPs alone is too large to support plasmonic coupling, and thus no transfer of energy is expected. The AgNP bridges this gap and transfers energy coherently between the two outer AuNPs, serving as a lossless virtual transmitting state (Fig. 1d). This can be understood as follows: if we excite our system in the gold plasmon resonance, the two gold plasmons are in resonance; however, at a distance too long to couple. At the same frequency, the silver plasmon is not in resonance but becomes involved as a quasi-resonant virtual state that operates as a transmitter. Since silver has a relatively small Drude dissipation constant, silver plasmons have a narrow plasmon peak and exhibit a very strong induced dipole moment even for relatively small NP sizes. These important features make AgNPs excellent transmitter elements that allow us to connect the two gold plasmons almost without dissipation, as we show in this study using both experiment and theory.

We characterized the plasmonic coherent transfer system with dark-field scattering spectroscopy of individual heterotrimers immobilized on a glass substrate in air, and compared the resulting spectra with theoretical calculations (see also Methods and Supplementary Information). Figure 2a displays the scattering spectra of several AuNP–AgNP–AuNP trimers in comparison to an Au–Au homodimer, missing the middle AgNP. The dominant resonance wavelength shifts from 549 nm for the AuNP homodimer to 586 nm for the heterotrimer structure. At the same time the peak intensity increases by a factor of approximately four. Apparently, the middle AgNP indeed serves as a connector to enable strong coupling between the two outer AuNPs. The experiments further show that the use of larger AgNPs results in a stronger dominant peak intensity at 586 nm. Concurrently, the resonance level of the AgNP becomes visible as a small peak at 445 nm.

The particle geometries in our numerical simulations were adjusted to the particle positions and sizes as determined from scanning electron microscopy (SEM) and TEM images. For the simulation of the dimer structure, two 40 nm AuNPs separated by a 38 nm gap were chosen. For the trimer simulations, a 30 nm AgNP was placed in the gap (see also Supplementary Figs 3 and 4). Figure 2b shows that the simulated scattering cross-sections are in excellent agreement with the observed spectra. For the heterotrimer, the dominant plasmon resonance peak shifts ~40 nm to the red. Furthermore, the peak intensity is increased by a factor of four compared to the homodimer. Most importantly, the simulations confirm that the AgNP does not dissipate energy at the resonance mode of the heterotrimer, but instead transfers the energy coherently between the two outer AuNPs (Fig. 2c).
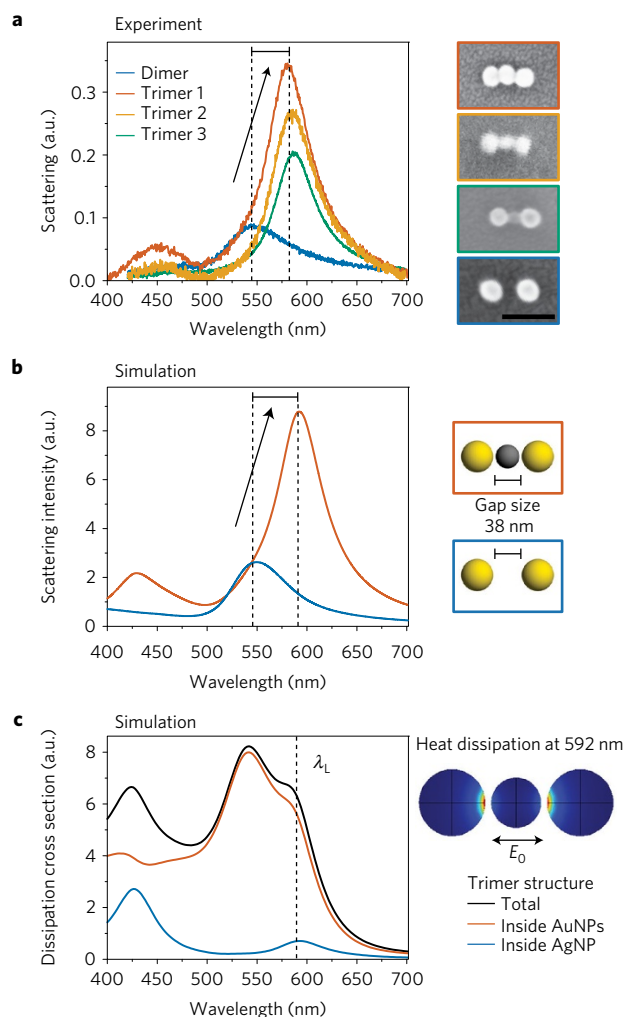

Figure 2 | Dark-field scattering spectra and simulations of the plasmonic transfer system. a, Single-structure scattering spectra of one homodimer and three heterotrimers and SEM images of the corresponding structures. Scale bar, 100 nm. A plasmon resonance shift of ~40 nm is observed. **b**, Numerical simulations for a homodimer structure of two 40 nm AuNPs with a 38 nm gap (blue) and for the same configuration with a 30 nm AgNP placed in the gap (orange). **c**, The simulated heat dissipation cross-section of the heterotrimers reveals that the AuNPs are dissipative at the resonance mode at $\lambda_L = 592$ nm, while the AgNP is not. The colour map shows the local heat dissipation in the longitudinal mode. Most of the dissipation appears in the hotspots on the AuNPs.
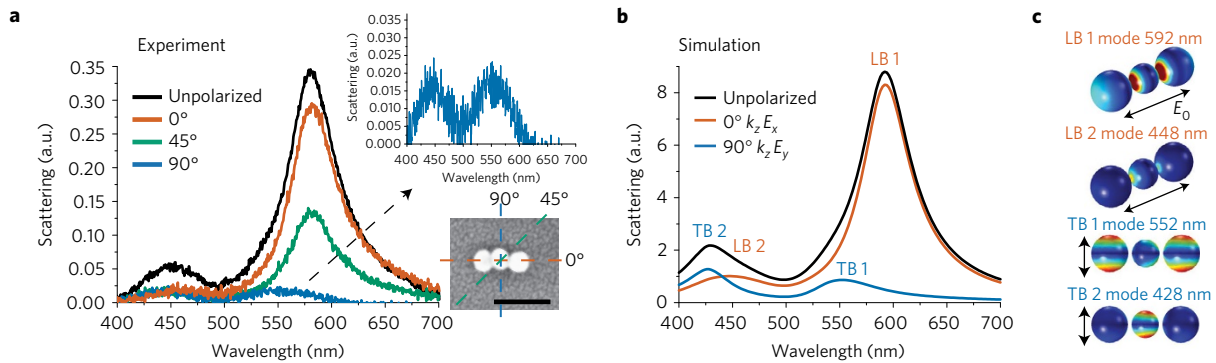
Figure 3 | Polarization-resolved measurements and calculations. a, Polarization-resolved scattering spectra of a heterotrimer structure. Only the resonances of uncoupled AuNPs and single AgNPs are detectable at 90° orientation of the polarizer in the detection path. The resonant mode appears in a parallel orientation of the polarizer. Inset: Orientations of the polarizer in respect to the trimer. Scale bar, 100 nm. **b,c,** Simulated polarization-resolved scattering spectra (**b**) and surface charge maps corresponding to the longitudinal and transversal bright modes (LB, TB) (**c**) are in excellent agreement with the experimental results.

Polarization-resolved scattering measurements give additional insight into this non-dissipative passage. Figure 3a shows such measurements for a single heterotrimer. For the linear detecting polarizer set to 90° with respect to the long trimer axis, only small transversal resonance peaks of the single AgNP and AuNPs are visible at ∼450 nm and ∼550 nm, respectively. At parallel (0°) polarization, the coupled, red-shifted mode appears. Our simulations fully reproduce these observations (Fig. 3b).

The charge colour maps in Fig. 3c display the key feature of the plasmon coupling in our structures: The energy transfer between the AuNPs occurs via the plasmonic hotspots formed in the Au–Ag gaps (see also Supplementary Fig. 5). These highly localized hotspots generate surface charges involving high multipole harmonics, which contrasts the standard picture for energy transfer processes between, for example, dye molecules.

By analysing the data in Fig. 2a,b, we can estimate the lifetime of the plasmon in the trimer and its transfer time between the two AuNPs. From the width of the plasmon peak we obtain a lifetime of ∼8 fs. From the splitting of the L-plasmon resonances (Δ_{splitt}) we calculate that $\tau_{\text{transfer}} \sim \pi/(2 \cdot \Delta_{\text{splitt}}) \sim 4.7$ fs (see Supplementary Notes and Supplementary Fig. 6). Exact electromagnetic simulations of the plasmon transfer dynamics support this analytical estimate. For this we placed an exciting dipole sending an 8.3-fs-long Gaussian pulse near one of the AuNPs and observed the dipolar moments of both AuNPs over time (Fig. 4). The electric dipole moments and the energies stored on the AuNPs show time-oscillating traces, and thus coherent transfer via the AgNP with a characteristic transfer time of ∼5 fs (Fig. 4 and Supplementary Figs 7 and 8). No such oscillations occur in the absence of the middle particle (Supplementary Fig. 9). As expected, the energy dissipation in the central transmitting AgNP is small, which shows the low-loss mechanism of information and energy transfer between the AuNPs mediated by the virtual silver plasmon. In summary, the observed plasmon lifetime and transfer time are both on the femtosecond timescale, enabling efficient and coherent transfer. Due to the strong coupling of the plasmonic dipoles, this process is orders of magnitude faster than FRET, which achieves only picosecond times both in plants and between FRET dyes in the lab[31]. In principle, FRET in molecules and semiconductor nanocrystals can be accelerated by plasmons, but only at the cost of high losses in the metal component[32].

As our structure is describable as a system of coupled oscillators, we can also apply a quantum model of the plasmonic excitations that should yield similar qualitative results. In this model the plasmons in the three NPs are considered as three quantum oscillators that are coupled by Coulomb forces and have each three degrees of freedom (Fig. 5a)[33]. To keep the calculations simple, we assume the
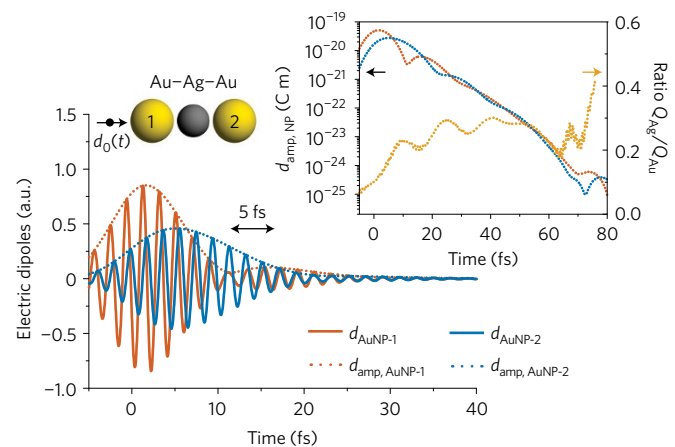

Figure 4 | Full electromagnetic simulations of the plasmon transfer dynamics. We placed a dipole sending a short Gaussian excitation pulse with a duration of 8.3 fs (FWHM) and a central frequency of $\hbar\omega = 2.21$ eV closely to one AuNP and monitored the dipoles in both AuNPs. Solid lines show the dipole oscillation in the left (orange) and in the right (blue) particle; dotted lines indicate the time variation of the amplitudes (envelope functions) of the corresponding NP dipoles. Inset: Dipole oscillations in both particles (blue and orange lines) and the ratio $Q_{\text{Ag}}/Q_{\text{AU}}$ between the dissipations in the two AuNPs and in the mediating AgNP (yellow line). The dissipation in the Ag mediator is small at all times. Oscillations between both Au particles indicate coherent transfer with an estimated transfer time of 5 fs.

dipolar limit for the plasmons, which, of course, underestimates the strength of coupling in our real samples. The total number of modes is 9 and the modes can be bright (B) or dark (D) and longitudinal (L) or transverse (T). They further exhibit certain degeneracies (see Fig. 5a and Supplementary Information for details and model parameters). The Hamiltonian of the coupled plasmonic oscillators reads

$$\hat{H} = \sum_{\alpha} \hbar\omega_{p,\alpha} \left(\hat{c}_{\alpha}^{\dagger}\hat{c}_{\alpha} + \frac{1}{2} \right) + \hat{H}_{\text{int}} \qquad (1)$$

where α is the index of each possible plasmonic state of isolated NP. The quantum index can be represented as $\alpha = (i, \gamma)$, where $i = 1, 2, 3$ is the NP number and $\gamma = x, y, z$ is the direction of oscillation. In equation (1), $\omega_{p,\alpha}$ and $\hat{H}_{\text{int}}$ are the plasmon frequencies of isolated NPs and the Coulomb coupling operator, respectively. The Hamiltonian (1) can be easily diagonalized and the spectrum
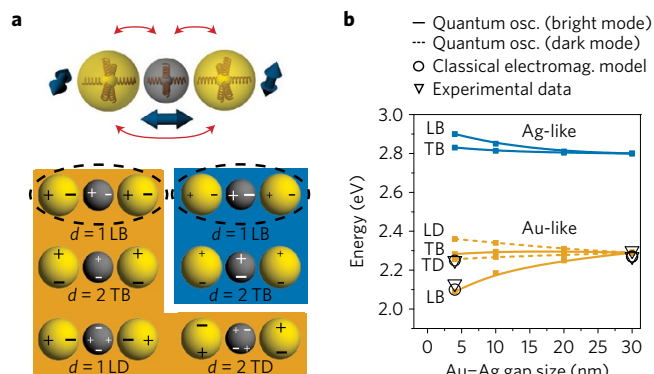
a

b

- — Quantum osc. (bright mode)
- ··· Quantum osc. (dark mode)
- ○ Classical electromag. model
- ▽ Experimental data

Figure 5 | Quantum model. a, Scheme displaying the harmonic-oscillator model of the plasmonic passage (top) and classification of the plasmonic modes (bottom). The main contributing mode to the plasmon passage and the mode assisting the passage of Au plasmons are circled with dashed lines. The label d denotes the degeneracy of the quantum plasmonic states. **b**, Energies of the different plasmonic modes calculated via the quantum oscillator model (solid and dashed lines), simulated by the classical electromagnetic model (circles) and experimentally obtained bright modes (triangles).

of vibrations can be found. The most interesting modes are the collective longitudinal ones:

$$\omega_{LB,Au\text{-like}} = \omega_{p,Au} - \Delta_{LB,Au}$$

$$\omega_{LD,Au\text{-like}} = \omega_{p,Au} + \Delta_{LD,Au}$$

$$\omega_{LB,Ag\text{-like}} = \omega_{p,Ag} + \Delta_{LB,Ag} \qquad (2)$$

where the positive parameters Δ are the energy shifts that appear in the spectrum due to the Au–Au and Au–Ag plasmonic interactions.

This relatively simple quantum model reproduces qualitatively the main important features of our experimentally and computationally obtained spectra (Fig. 5b), which makes this one of the rare examples where classical and quantum pictures are equivalent when considering the coherent properties of coupled plasmons. In particular, the quantum model reproduces the red shift of the main Au-like L-plasmon, the appearance of splittings in the spectra, and a larger splitting for the L-modes as compared to the T-modes. Again, we observe that the silver plasmon plays the role of a mediator for the enhanced coupling between the two gold plasmons. Despite the drastic simplification of our quantum model, which ignores multipolar modes, the formation of hotspots and some other fine details of the system, it helps to understand all plasmonic modes and the characteristic spectral shifts.

Our heterogeneous particle chain where, in contrast to conventional homogeneous mono-metallic waveguides, a silver nanoparticle is introduced as a coherent transmitter allows for ultrafast excitation transfer with almost no losses in the transmitting element. Advanced experimental methods such as nonlinear time-resolved femtosecond spectroscopy in a pump–probe setup could in future studies record the coherent plasmonic dynamics of the Au–Ag–Au trimer. In a nonlinear plasmonic regime and employing methods of quantum spectroscopy, such a trimer can become a model system to create and control pairs of plasmonic quanta (qubits) and their quantum entangled states, as is currently done for photons and electrons.

Methods

Methods, including statements of data availability and any associated accession codes and references, are available in the online version of this paper.

References

1. Greentree, A. D., Cole, J. H., Hamilton, A. R. & Hollenberg, L. C. L. Coherent electronic transfer in quantum dot systems using adiabatic passage. *Phys. Rev. B* **70,** 235317 (2004).
2. Rech, J. & Kehrein, S. Effect of measurement backaction on adiabatic coherent electron transport. *Phys. Rev. Lett.* **106,** 136808 (2011).
3. Aharonovich, I., Greentree, A. D. & Prawer, S. Diamond photonics. *Nat. Photon.* **5,** 397–405 (2011).
4. Ozbay, E. Plasmonics: merging photonics and electronics at nanoscale dimensions. *Science* **311,** 189–193 (2006).
5. Akimov, A. V. *et al*. Generation of single optical plasmons in metallic nanowires coupled to quantum dots. *Nature* **450,** 402–406 (2007).
6. Pal, S., Deng, Z., Ding, B., Yan, H. & Liu, Y. DNA-origami-directed self-assembly of discrete silver-nanoparticle architectures. *Angew. Chem.* **122,** 2760–2764 (2010).
7. Alivisatos, A. P. *et al*. Organization of 'nanocrystal molecules' using DNA. *Nature* **382,** 609–611 (1996).
8. Zheng, J. *et al*. Two-dimensional nanoparticle arrays show the organizational power of robust DNA motifs. *Nano Lett.* **6,** 1502–1504 (2006).
9. Kuzyk, A. *et al*. DNA-based self-assembly of chiral plasmonic nanostructures with tailored optical response. *Nature* **483,** 311–314 (2012).
10. Gopinath, A., Miyazono, E., Faraon, A. & Rothemund, P. W. K. Engineering and mapping nanocavity emission via precision placement of DNA origami. *Nature* **535,** 401–405 (2016).
11. Bergmann, K., Theuer, H. & Shore, B. W. Coherent population transfer among quantum states of atoms and molecules. *Rev. Mod. Phys.* **70,** 1003–1025 (1998).
12. Vitanov, N. V., Halfmann, T., Shore, B. W. & Bergmann, K. Laser-induced population transfer by adiabatic passage techniques. *Annu. Rev. Phys. Chem.* **52,** 763–809 (2001).
13. Maier, S. A. *et al*. Local detection of electromagnetic energy transport below the diffraction limit in metal nanoparticle plasmon waveguides. *Nat. Mater.* **2,** 229–232 (2003).
14. Seeman, N. C. Nanomaterials based on DNA. *Annu. Rev. Biochem.* **79,** 65–87 (2010).
15. Schreiber, R. *et al*. Hierarchical assembly of metal nanoparticles, quantum dots and organic dyes using DNA origami scaffolds. *Nat. Nanotech.* **9,** 74–78 (2014).
16. Mastroianni, A. J., Claridge, S. A. & Alivisatos, A. P. Pyramidal and chiral groupings of gold nanocrystals assembled using DNA scaffolds. *J. Am. Chem. Soc.* **131,** 8455–8459 (2009).
17. Roller, E.-M., Argyropoulos, C., Högele, A., Liedl, T. & Pilo-Pais, M. Plasmon–exciton coupling using DNA templates. *Nano Lett.* **16,** 5962–5966 (2016).
18. Klein, W. P. *et al*. Multiscaffold DNA origami nanoparticle waveguides. *Nano Lett.* **13,** 3850–3856 (2013).
19. Ding, B. *et al*. Gold nanoparticle self-similar chain structure organized by DNA origami. *J. Am. Chem. Soc.* **132,** 3248–3249 (2010).
20. Roller, E.-M. *et al*. DNA-assembled nanoparticle rings exhibit electric and magnetic resonances at visible frequencies. *Nano Lett.* **15,** 1368–1373 (2015).
21. Stein, I. H., Schüller, V., Böhm, P., Tinnefeld, P. & Liedl, T. Single-molecule FRET ruler based on rigid DNA origami blocks. *ChemPhysChem* **12,** 689–695 (2011).
22. Sharma, J. *et al*. DNA-tile-directed self-assembly of quantum dots into two-dimensional nanopatterns. *Angew. Chem. Int. Ed.* **47,** 5157–5159 (2008).
23. Fu, A. *et al*. Discrete nanostructures of quantum dots/Au with DNA. *J. Am. Chem. Soc.* **126,** 10832–10833 (2004).
24. Lee, J.-H., Kim, G.-H. & Nam, J.-M. Directional synthesis and assembly of bimetallic nanosnowmen with DNA. *J. Am. Chem. Soc.* **134,** 5456–5459 (2012).
25. Pal, S., Sharma, J., Yan, H. & Liu, Y. Stable silver nanoparticle-DNA conjugates for directed self-assembly of core-satellite silver-gold nanoclusters. *Chem. Commun.* 6059–6061 (2009).
26. Xu, L., Tan, L. S. & Hong, M. H. Tuning of localized surface plasmon resonance of well-ordered Ag/Au bimetallic nanodot arrays by laser interference lithography and thermal annealing. *Appl. Opt.* **50,** G74–G79 (2011).
27. Shegai, T. *et al*. A bimetallic nanoantenna for directional colour routing. *Nat. Commun.* **2,** 481 (2011).
28. Rothemund, P. W. K. Folding DNA to create nanoscale shapes and patterns. *Nature* **440,** 297–302 (2006).
29. Douglas, S. M. *et al*. Self-assembly of DNA into nanoscale three-dimensional shapes. *Nature* **459,** 414–418 (2009).
30. Douglas, S. M. *et al*. Rapid prototyping of 3D DNA-origami shapes with caDNAno. *Nucleic Acids Res.* **37,** 5001–5006 (2009).
31. May, V. & Kühn, O. *Charge and Energy Transfer Dynamics in Molecular Systems* Vol. 3 (John Wiley, 2011).

32. Govorov, A. O., Lee, J. & Kotov, N. A. Theory of plasmon-enhanced Förster energy transfer in optically excited semiconductor and metal nanoparticles. *Phys. Rev. B* **76,** 125308 (2007).
33. Otten, M. *et al*. Entanglement of two, three, or four plasmonically coupled quantum dots. *Phys. Rev. B* **92,** 125432 (2015).

Author contributions
E.-M.R., A.O.G. and T.L. conceived the experiments and co-wrote the manuscript. E.-M.R. designed the structure and analysed the data. E.-M.R. and C.P. performed the experiments. L.V.B. and L.K.K. performed the simulations, A.O.G. developed the quantum model. All authors contributed to the interpretation and general discussion and reviewed the manuscript.

Additional information
Supplementary information is available in the online version of the paper. Reprints and permissions information is available online at www.nature.com/reprints. Publisher's note: Springer Nature remains neutral with regard to jurisdictional claims in published maps and institutional affiliations. Correspondence and requests for materials should be addressed to A.O.G. or T.L.

Competing financial interests
The authors declare no competing financial interests.

Methods

Assembly of heterogeneous particle trimer structures. *DNA origami folding.* In DNA origami, a ~8,000-nucleotide-long viral single-stranded DNA (ssDNA) scaffold is folded into a programmed shape with the help of ~200 short, synthetic ssDNA staple strands. Due to the sequence-defined assembly of the DNA structure, the location of each staple strand and each DNA base within the structure is exactly defined. By extending a selected subset of the staple strands with tailored anchor sequences, the folded DNA origami structure can be employed as a breadboard exhibiting unique and sequence-specific binding sites for DNA-modified metal nanoparticles. Our DNA origami structure offers two outer attachment sites with the same DNA anchor sequence and a middle site with an orthogonal sequence. The DNA origami 14-helix bundle (14hB) was folded using 10 nM of the scaffold p8634, 100 nM of each staple strand, 10 mM Tris, 1 mM EDTA (pH 8) and 16 mM $MgCl_2$. This mixture was heated to 65 °C for 20 min and then slowly cooled down to 20 °C over a period of 40 h. Specific staple strands at the attachment site were elongated by either 15× A bases for AuNP attachment or by the sequence ATG TAG GTG GTA GAG AA for AgNP attachment. Thus, each attachment site consists of five single-stranded extensions of staples whose ends are located close to each other on the surface of the origami structure. The extended staple strands are labelled in Supplementary Fig. 1 with red colour. All the staples for nanoparticle attachment via DNA hybridization were already included into the folding solution according to the targeted final NP–DNA origami structure (trimer or dimer structure). After folding the structures, a purification step with a 1% agarose gel in 1× TAE (40 mM Tris, 40 mM Acetic Acid, 1 mM EDTA, pH 8) containing 11 mM $MgCl_2$ was performed. The band containing the structures was cut out from the gel with a razor blade. The DNA origami structures were recovered with a pipette while squeezing the gel band between two glass slides. The concentration of the 14-helix bundle after purification was determined via ultraviolet–visible (UV–Vis) spectroscopy (Nanodrop).

Concentration of AuNPs and conjugation with DNA. First, 40 nm AuNPs (BBI Solutions, 20 ml) were concentrated using the protocol of Schreiber and colleagues[12]. The AuNPs were mixed with 8 mg BSPP (Bis(*p*-sulfonatophenyl)phenylphosphine dihydrate dipotassium salt, Sigma-Aldrich) and shaken for three days. Afterwards NaCl was added until a colour change to blue was observed. Then the solution was centrifuged at 1,600 rcf for 30 min and the supernatant discarded. Next, 1 ml of 2.5 mM BSPP in H_2O and 1 ml Methanol was added. After vortexing, the solution was centrifuged again at 1,600 rcf for 30 min and the supernatant was discarded. The concentrated AuNPs were redissolved in 200 μl 2.5 mM BSPP and their concentration was determined via UV–Vis spectroscopy (Nanodrop). The following functionalization of the AuNPs with 5′ thiol-modified ssDNA strands (Biomers.net, 19× T bases) has two goals: first, the DNA coverage of the AuNPs renders them stable against high $MgCl_2$ concentrations as they are used within the DNA origami folding process. Second, the sequence of the thiol-modified ssDNA strands is chosen to be complementary to the single-stranded extensions of the staple strands that together form the AuNP attachment sites on the 14-helix bundle structure. Thus the AuNPs can hybridize to the predesigned sites on the DNA origami structure. For the functionalization a ratio of AuNPs:thiol ssDNA of 1:5,000 was used. 0.5× TBE buffer was added to the AuNPs and the ssDNA and the solution was kept on a shaker for three days. Afterwards a purification step was performed to get rid of the unbound ssDNA strands. For that the AuNPs were run over a 100 kDa molecular weight cutoff (MWCO) centrifugal filter (Amicon Ultra, Millipore, 5 min, 8,000 rcf) followed by additional eight centrifugation steps with a filter exchange after four steps. This purification from unbound ssDNA strands is crucial to avoid blocking of the attachment sites on the DNA origami structure by free complementary ssDNA strands. Best yields of AuNPs-to-DNA-origami binding can be achieved if the last centrifugation steps are performed directly before mixing the AuNPs with the DNA origami structures.

AgNPs functionalization with DNA. For the functionalization of AgNPs with ssDNA a 5′ thiol-modified sequence TTC TCT ACC ACC TAC AT (biomers.net) was used. A functionalization sequence that is different to the AuNP sequence guarantees that the attachment of AuNPs and AgNPs to the 14-helix bundle is specific. First, the as-purchased AgNPs (Cytodiagnostics, 50 nm, 1 ml) were mixed with the sequence (40 μl, 100 μM stock concentration) and 1× TE buffer. This solution was kept protected from light on a shaker for one week. Afterwards NaCl

ageing was performed by slowly raising the NaCl concentration to 100 mM over the course of one day. Then short 5′ thiol-modified ssDNA (5x T, MWG eurofins, 20 μl, 1 mM stock concentration) were added. This short DNA strand is used as 'back filler' to assure high $MgCl_2$ stability of the AgNPs while it is too short to hybridize to the DNA origami structure. The solution was left again over night for incubation. Then the NaCl concentration was raised to a final concentration of 500 mM over the course of 6 h. As the last step, the DNA-functionalized AgNPs were purified from excess unbound ssDNA strands by using 100 kDa MWCO centrifugal filters as described in the AuNPs procedure.

Functionalization of DNA origami 14-helix bundle structure with AuNPs and AgNPs. After determining the concentration of the DNA-modified AgNPs and AuNPs via UV–Vis spectroscopy, they were mixed together with the purified DNA origami 14-helix bundle template. This structure offers two attachment sites for AuNPs and one attachment site for AgNPs. Each attachment site consists of five elongated staple strands offering the complementary sequence to the corresponding metal nanoparticle. The DNA origami structure and the metal nanoparticles were mixed in a ratio attachment site:AuNP/AgNP of 1:4. The excess of metal nanoparticles over attachment sites ensures high binding yields and prevents crosslinking of origami structures mediated by nanoparticles. After overnight incubation of the solution, a 0.7% agarose gel electrophoresis in 1× TAE and 11 mM $MgCl_2$ buffer was run to separate the desired heterogeneous trimer structures from excess, unbound metal nanoparticles and from aggregates (Supplementary Fig. 2). The band containing the trimer structures was excised from the gel and the nanostructures extracted by squeezing the cut gel band between two glass slides. The solution received in a pipette contained the purified final trimer structures.

Characterization of heterogeneous particle trimer structures. *Transmission electron microscopy (TEM).* TEM was used to control the correct assembly of the particle trimer nanostructures. A droplet of the solution containing the purified structures was deposited on a plasma-exposed carbon-formvar-coated TEM grid (Ted Pella) and then dabbed off after 3 min. The grid was stained with 1% uranyl formate for 15 s. Imaging was performed with a JEOL JEM-1100 at an acceleration voltage of 80 kV.

Dark-field scattering spectroscopy. To take scattering spectra of single trimer structures the purified trimer solution was diluted 20× in 1× TAE buffer containing 11 mM $MgCl_2$ and immobilized on cleaned glass cover slides. Therefore, a droplet of the diluted solution was deposited for 5 min onto the glass slides, and then doubly distilled H_2O was rinsed over the slide to wash away salt residues. To avoid denaturation of the DNA structures, the slides were dried with a nitrogen flush immediately. The measurements were then performed in air. The dark-field scattering spectra were collected with a home-built dark-field setup in transmission mode using a 100× air objective (Olympus) and an oil condenser (Olympus NA 1.4) with a 100 W halogen bulb as illumination source coupled to an Acton SP2300 spectrometer (Princeton Instruments). Polarization-resolved scattering spectra were taken by exciting the system with unpolarized incident light and detecting the scattered light through a rotatable polarizer. Scattering spectra of single AuNP dimer structures (no intermediate AgNP) and single AuNP-AgNP dimer structures[34] (only one outer AuNP) were performed accordingly. The spectra are shown in Supplementary Figs 3 and 4.

Scanning electron microscopy (SEM). The single structures characterized in the dark-field setup were further analysed by SEM. Therefore, the glass slides were subsequently sputtered with a 3 nm gold palladium layer and imaged using a Gemini Ultra Plus field emission SEM (Zeiss). The images were taken using the in-lens detector and an electron acceleration voltage of 2 kV at a working distance of 3.0 mm.

Data availability. The data that support the plots within this paper and other findings of this study are available from the corresponding author upon reasonable request.

References

34. Weller, L. *et al*. Gap-dependent coupling of Ag–Au nanoparticle heterodimers using DNA origami-based self-assembly. *ACS Photon.* **3,** 1589–1595 (2016).